Study of electron acceleration and x-ray radiation as a function of plasma density in capillary-guided laser wakefield accelerators

J. Ju, K. Svensson, H. Ferrari, A. Döpp, G. Genoud, F. Wojda, M. Burza, A. Persson, O. Lundh, C.-G. Wahlström, and B. Cros

Citation: Physics of Plasmas (1994-present) **20**, 083106 (2013); doi: 10.1063/1.4817747
View online: http://dx.doi.org/10.1063/1.4817747
View Table of Contents: http://scitation.aip.org/content/aip/journal/pop/20/8?ver=pdfcov
Published by the AIP Publishing

Study of electron acceleration and x-ray radiation as a function of plasma density in capillary-guided laser wakefield accelerators

J. Ju,[1] K. Svensson,[2] H. Ferrari,[3] A. Döpp,[1] G. Genoud,[2] F. Wojda,[2] M. Burza,[2] A. Persson,[2] O. Lundh,[2] C.-G. Wahlström,[2] and B. Cros[1,a)]
[1]*Laboratoire de Physique des Gaz et des Plasmas, CNRS-Université Paris-Sud, 91405 Orsay, France*
[2]*Department of Physics, Lund University, P.O. Box 118, S-22100 Lund, Sweden*
[3]*Consejo Nacional de Investigaciones Científicas y Técnicas (CONICET) and CNEA-CAB, Argentina*

(Received 3 May 2013; accepted 15 July 2013; published online 6 August 2013)

Laser wakefield electron acceleration in the blow-out regime and the associated betatron X-ray radiation were investigated experimentally as a function of the plasma density in a configuration where the laser is guided. Dielectric capillary tubes were employed to assist the laser keeping self-focused over a long distance by collecting the laser energy around its central focal spot. With a 40 fs, 16 TW pulsed laser, electron bunches with tens of pC charge were measured to be accelerated to an energy up to 300 MeV, accompanied by X-ray emission with a peak brightness of the order of 10^{21} ph/s/mm^2/mrad^2/0.1%BW. Electron trapping and acceleration were studied using the emitted X-ray beam distribution to map the acceleration process; the number of betatron oscillations performed by the electrons was inferred from the correlation between measured X-ray fluence and beam charge. A study of the stability of electron and X-ray generation suggests that the fluctuation of X-ray emission can be reduced by stabilizing the beam charge. The experimental results are in good agreement with 3D particle-in-cell (PIC) simulation. © *2013 AIP Publishing LLC*. [http://dx.doi.org/10.1063/1.4817747]

I. INTRODUCTION

Laser wakefield acceleration (LWFA) is a mechanism with a high potential for the development of compact electron and radiation sources and accelerating structures scalable to high electron energy. A few decades ago, relativistic plasma waves driven by intense laser pulses were proposed as means to accelerate electrons due to the ultra-high longitudinal electric field that can be sustained by a plasma.[1] Since then, laser wakefield acceleration mechanisms have been investigated theoretically, numerically, and experimentally, and remarkable progress has been made worldwide.[2] A first breakthrough was achieved in 2004 when the generation of peaked electron distributions with an energy of ~100 MeV was demonstrated.[3–5] Subsequently, electrons at the 1 GeV level were reported in an experiment where the acceleration length was extended with a plasma channel to a few centimeters.[6] In LWFA, plasma wave excitation relies on the ponderomotive force of a short, intense laser pulse expelling electrons out of the high laser intensity regions. For high enough laser intensity, typically above 10^{18} W/cm^2, plasma electrons can be completely expelled out of the intense laser volume and self-trapped in the accelerating potential of the plasma wave.[7] In addition to the accelerating fields associated with the plasma wave, the accelerated electrons experience transverse fields. Thus, these electrons can undergo strong transverse oscillations, known as betatron oscillations, giving rise to the emission of synchrotron-like radiation, which has been studied theoretically[8,9] and observed experimentally.[10–13] This X-ray source is very attractive for applications to time-resolved imaging due to its compactness and its intrinsic properties as it is spatially coherent, brilliant, with duration as short as a few femtoseconds, and perfectly synchronized to the pump laser.[11]

The plasma density and length are key parameters to control the laser plasma interaction regime and therefore the regime of operation of the accelerator. Laser wakefield excitation in long plasmas is of interest either in the blow-out regime, where simulations[7] show that using long plasmas at relatively low densities is a way to achieve electron acceleration to the multi-GeV range and beyond, or in the more linear acceleration regime[14] for multi-stage acceleration. To achieve low density plasmas, and guide the intense laser over a long enough distance, using capillary tubes[15] has several advantages:[16] the plasma density inside capillary tubes can be arbitrarily low, as the laser beam is guided by reflection from the tube walls and there is no density requirement for guiding, so that different plasma density ranges can be explored; the capillary tube provides a shock-free gas medium, beneficial for generating stable electrons[17] and X-rays; the capillary tube is able to collect part of the laser energy in the wings around the central focal spot to assist laser guiding over a longer distance than in a gas jet or gas cell.[18,19] Especially in the case of laser guiding by capillary tubes with radius larger than twice the waist of the focal spot, nearly all the laser energy can be collected by the interplay of self-focusing and reflection from the capillary wall, leading to a higher laser peak intensity and longer distance of self-focusing than in a medium without boundary. Electron self-injection near threshold and acceleration inside capillary tubes were observed previously with a moderately intense laser.[18–20] Operating around the threshold of self-injection, electrons were observed only in a narrow density regime,[19] and the photon energy (~1 keV) and X-ray fluence was lower than 1×10^5 ph/mrad^2.

In this paper, we present a study of electron self-injection in long plasmas produced inside capillary tubes for a value of

a)Electronic mail: brigitte.cros@u-psud.fr

the input laser intensity around 5.4×10^{18} W/cm^2. Highlights from the same experiment were published previously;[21] here a detailed analysis is presented, including simulation results. The influence of the plasma density and of the capillary tube parameters on electron energy, beam charge, electron self-trapping, and X-ray intensity are characterized using the measured electron and X-ray beams. The X-ray profile is geometrically related to the emission positions in the plasma by the rim of the capillary exit and provides a good probe of the acceleration process. We also address the stability of the accelerated electrons and the corresponding X-ray radiation. Those results are compared with numerical particle-in-cell (PIC) simulation results obtained with the code CALDER-CIRC.[22]

II. EXPERIMENT

A. Experimental setup

An experiment was carried out with the multi-terawatt laser at the Lund Laser Centre (LLC) in Sweden. The titanium-doped sapphire (Ti:Sa) laser operates in the chirped pulse amplification mode and was able to deliver a laser pulse with an energy of 650 mJ at 800 nm central wavelength on target, and a FWHM pulse duration of 40 fs. Figure 1 illustrates the experimental setup. The laser beam was focused 1 mm inside the capillary tubes by a $f = 76$ cm off-axis parabola. Using a motorized holder composed of three translation and two rotation stages, capillary tubes were aligned on the laser axis. The capillary tubes are made of glass: their inner surface is optically smooth at the laser wavelength, and their walls are thick, with an external diameter of 5.5 mm. Hydrogen gas was filled into the capillary tubes through two ~270 μm wide slits situated at 2.5 mm from each capillary end. The plasma density inside the capillary tubes was adjusted by a gas regulator controlling the upstream reservoir pressure.[23] A 10 cm long permanent magnet with a central field of 0.7 T over a 15 mm gap deflected electrons downwards onto a scintillating (Kodak Lanex Regular) screen which was imaged by a 12-bit charge-coupled device (CCD) camera. Electrons with energies below 42 MeV could not reach the Lanex screen and were thus not recorded. The Lanex screen was protected by an aluminum shield from direct exposure to the laser light, and a narrow-band interference filter (IF) was placed in front of the CCD camera to reduce background light. A tracking code was developed to retrieve electron spectra from the raw images of Lanex, and the beam charge was evaluated from the absolute calibration of Lanex.[24,25] The beam charge shown in Ref. 21 was underestimated by a factor of ~2.3 owing to an incorrect determination of the transmission of the IF filter. Corrected values are given in this paper. On the same laser shots, the far-field betatron radiation was also recorded using a 16-bit X-ray CCD camera placed about 110 cm away from the capillary exit. This camera has a 13×13 mm^2 chip, corresponding to a collecting angle of 12×12 mrad^2. A set of thin metallic filters (Zr: 3 μm, Sn: 3 μm, V: 3 μm, Fe: 3 μm, Ni: 5 μm) with different X-ray absorption edges was inserted in front of the X-ray camera to allow an estimation of the photon spectra. Two beryllium windows with a total thickness of 300 μm and a 5 mm air gap in the X-ray path in front of the X-ray camera prevented detection of photons with energy less than 2 keV.

The energy distribution in the transverse plane delivered by the laser system exhibits a nearly flat-top cylindrically symmetrical distribution before focusing. In the focal plane, the corresponding energy distribution is close to an Airy distribution, as shown in Fig. 2. The focal spot shown in Fig. 2(a) was obtained by tuning a deformable mirror placed after the compressor to compensate for aberrations in the laser wavefront. The average radius of the focal spot at the first minimum can be determined from the radial profile of energy distribution averaged over the angles to be 19.7 ± 0.8 μm, which yields an on-axis peak intensity of $(5.4 \pm 0.1) \times 10^{18}$ W/cm^2 and a normalized laser vector potential of $a_0 \simeq 1.6$. The energy fraction contained within the grey shaded area in Fig. 2(b) is estimated to be equal to about 43% of the laser energy in the focal plane, which is comparable with the theoretical prediction of ~47% energy within FWHM for an Airy distribution.

The capillary tubes employed in this experiment range from 152 μm to 254 μm in diameter and 10 mm to 30 mm in length. For the focal spot shown in Fig. 2, the focal spot diameter at the first minimum over capillary diameter ratio is in the range 0.26 to 0.16 and gives rise to multimode[15] excitation at the entrance of the capillary tubes.

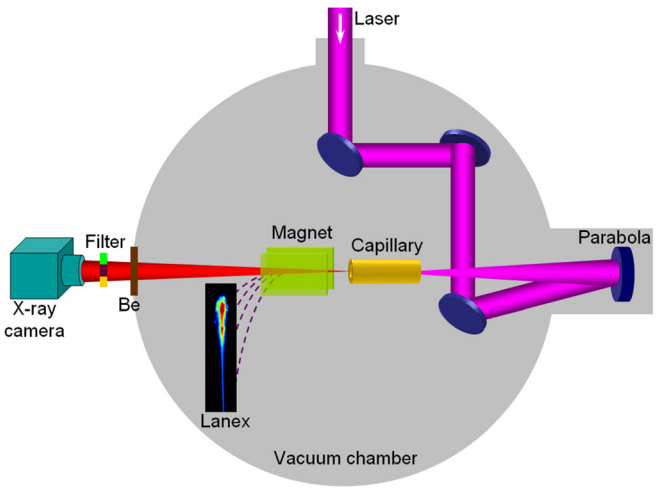

FIG. 1. Schematic diagram of the experimental arrangement. Elements inside the grey area are under vacuum. The Lanex screen shows a typical energy spectrum of the accelerated electrons obtained in experiment.

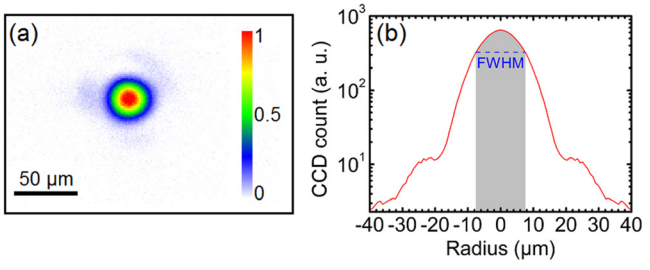

FIG. 2. (a) Energy distribution in the focal plane normalized to its maximum, (b) averaged radial profile of laser energy in logarithmic scale. The energy in the grey shaded area, of diameter equal to FWHM, represents about 43% of the laser energy in the focal spot.

B. Electron acceleration

Over the whole capillary parameter range explored, electron beams with charge in the range 1 to 150 pC were observed, and the electron spectra were found to sensitively depend on plasma density. As mentioned previously, the beam charge determined experimentally takes into account electrons with an energy above the detector lower limit of 42 MeV. Examples of energy spectra, obtained for a 10 mm long capillary with a diameter of 178 μm, are shown in Fig. 3 for two different values of the plasma electron density; raw Lanex images are shown in panels (a) and (c), while the corresponding spectra are plotted in (b) and (d) after summing in the transverse direction and rescaling to account for magnet dispersion. Accelerated electrons with a maximum energy of 300 MeV and a charge of ~2 pC were obtained for a plasma density $n_e = (5.4 \pm 0.3) \times 10^{18}\,\mathrm{cm}^{-3}$ as shown in Figs. 3(a) and 3(b). The maximum energy is defined when the energy spectrum decreases to 10% of its peak value. The electron beam FWHM divergence in the case of Fig. 3(b) is about 5.2 mrad. It was found that at such a low plasma density, the electron beam properties exhibit large shot-to-shot fluctuations, due to the fact that LWFA operates just above the threshold of self-injection.[20] When a higher plasma density, $n_e = (8.1 \pm 0.5) \times 10^{18}\,\mathrm{cm}^{-3}$, was used electron beams with a higher charge were produced, about 40 pC for the example of Figs. 3(c) and 3(d). In this case, the maximum electron energy was limited to 120 MeV. Moreover, several structures are observed in the raw image of Fig. 3(c), which can be interpreted as resulting from multiple electrons trapping inside the bubble along the acceleration distance or electrons emergence from different plasma buckets.

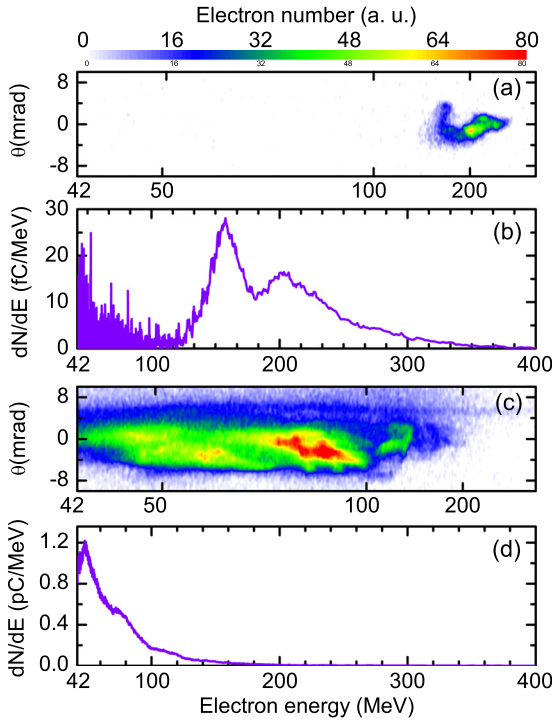

FIG. 3. Raw Lanex images and their corresponding energy spectra inside a 10 mm long, 178 μm diameter capillary tube at plasma electron densities: $(5.4 \pm 0.3) \times 10^{18}\,\mathrm{cm}^{-3}$ for (a)–(b) and $(8.1 \pm 0.5) \times 10^{18}\,\mathrm{cm}^{-3}$ for (c)–(d), respectively.[21]

In contrast to the narrow density range where self-electron trapping occurs at lower laser intensities, around $0.8 \times 10^{18}\,\mathrm{W/cm}^2$ in our previous experiments,[19,20] for the value of intensity used for the results presented in this paper, electrons were detected in a broad range of plasma densities above the threshold for self-injection, as shown in Fig. 4. In this figure, the maximum electron beam energy (a), and the charge estimated for the corresponding shots (b), are plotted as functions of the plasma electron density, inside a 10 mm long, 178 μm diameter capillary tube. The black squares are experimental results, each point corresponding to one single laser shot and error bars to the precision of the measurements.

Figure 4(a) shows that the highest value of maximum beam energy is achieved for the lowest value of electron density where self-injection occurs, and that the beam maximum energy decreases as the plasma density is increased, in agreement with previous findings.[3,26] The measured dependence of beam maximum energy behaves as $1/n_e$ and can be compared to the phenomenological scaling law developed for the 3D non-linear regime,[7] when the electron maximum energy is limited by dephasing: $\mathcal{E}\,[\mathrm{MeV}] = \frac{1}{3} a_0 n_c / n_e$, where n_c is the critical density. Dephasing occurs when an accelerated electron slips forward in the plasma wave and enters a decelerating phase; its characteristic length is given in this non-linear regime by $L_{dph} = \frac{4}{3}\sqrt{a_0} n_c / (n_e k_p)$ where k_p is the plasma wave wavenumber. The experimental points are in a region of the graph limited by curves with values of a_0 in the range 1.1 to 2.6, which can be interpreted as effective values of a_0 over the whole plasma length. The point of highest electron energy in Fig. 4(a) corresponds to a curve with $a_0 = 2.6$. During the

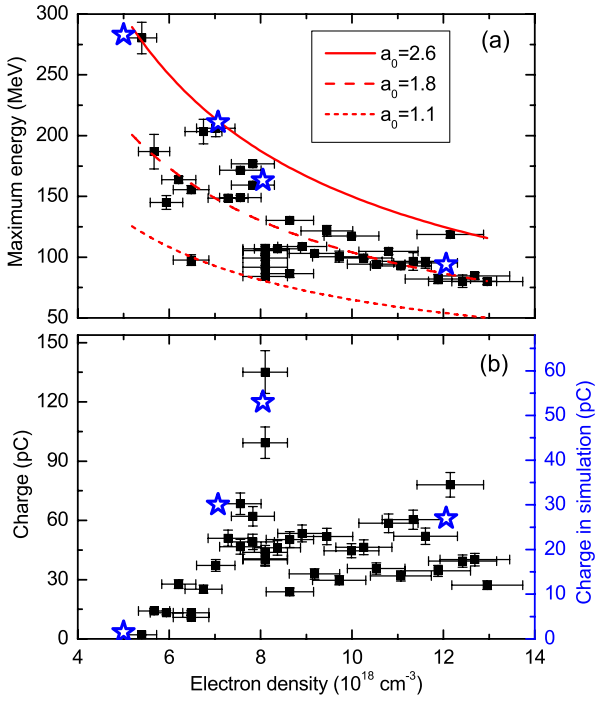

FIG. 4. (a) Maximum electron beam energy and (b) charge as a function of plasma electron density, at the output of a 10 mm long, 178 μm diameter capillary tube. The black squares are experimental results, each point corresponding to one single laser shot. Blue stars are the results of PIC simulations. The curves in (a) show the predictions of scaling laws obtained for the three values of a_0 indicated in the legend.

propagation in the plasma, the increase of laser intensity is linked to pulse compression and self-focusing as the incident power P is above $P_c[\mathrm{GW}] \simeq 17 n_c/n_e$, the critical power for self-focusing: $2.8P_c < P < 7.2P_c$. The maximum energy values measured agree with simulation results, plotted as blue stars, as will be presented in Sec. III.

The dephasing length L_{dph} is calculated to be about 1.6 mm for $n_e = 5.4 \times 10^{18}\,\mathrm{cm}^{-3}$. L_{dph} becomes shorter at higher plasma densities, and the capillary length, L_{cap}, was always longer than the dephasing length in this experiment. The electrons observed in this experiment were thus accelerated over the dephasing length and decelerated, so that their output energies are in general lower than the prediction of the scaling law. The electron maximum energy obtained by PIC simulation at the output of the capillary tube agrees well with experimental observations. At low density, the simulation data are consistent with the curve for $a_0 = 2.6$, while they start to deviate from it and approach the curve for $a_0 = 1.8$ as density increases, as the result of the shorter dephasing length and longer propagation distance inside the capillary beyond the dephasing length.

For plasma densities below $8 \times 10^{18}\,\mathrm{cm}^{-3}$, the measured electron energy exhibits larger shot-to-shot fluctuations than in the larger density range. This can be attributed to electron injection just above the threshold of self-trapping, observed previously[20] to be around $P/P_c \simeq 3.3$, corresponding here to a density of about $6 \times 10^{18}\,\mathrm{cm}^{-3}$.

Figure 4(b) shows that the beam charge reaches a maximum around the value of plasma density, $n_e = 8 \times 10^{18}\,\mathrm{cm}^{-3}$ in the experiment and the simulation. This observation can be understood as follows. Here, the characteristic depletion length of laser energy is given by $L_{dpl} = c\tau n_c/n_e$ and is larger than the dephasing length in the range of electron density studied. Electron injection and acceleration occur above the threshold and the amount of accelerated charge increases with the density, as the value of the ratio P/P_c is increased for a fixed incident laser power. The increase of accelerated charge above $n_e = 5 \times 10^{18}\,\mathrm{cm}^{-3}$ can be explained by more efficient electron self-trapping occurring for a higher ratio of P/P_c, as observed in Ref. 27 and by the decrease of the phase velocity of the plasma wave. For densities larger than $n_e = 8 \times 10^{18}\,\mathrm{cm}^{-3}$, the dephasing and pump depletion length being less than 1 mm and 2 mm, respectively, in this range of plasma density, some electrons are scattered during the propagating in the remaining part of the plasma,[28] roughly 5 mm long, and do not reach the detector. The main contribution to the difference of beam charge in simulation and experiment is due to electrons going out from the simulation box. The simulation box [as seen in Fig. 12(c)] moves forward with the group velocity of the laser in the plasma $v_g \simeq 0.998c$, while the accelerated electrons in the first plasma bucket move nearly with speed of light c, so more and more electrons overrun the front boundary of the simulation box and get lost with computation time increasing, leading to the observed lower beam charges in simulation.

C. Betatron radiation

In the regime of acceleration described in Sec. I, trapped electrons, if injected off-axis or with some transverse momentum, oscillate transversely during acceleration and generate intense X-ray emission, often referred to as betatron radiation.[10] A relativistic electron with a total energy of $\gamma m_e c^2$ wiggles at the betatron frequency $\omega_\beta = \omega_p/\sqrt{2\gamma}$, where ω_p is the plasma frequency. The radiated spectrum is determined by the strength parameter $K = \gamma r_\beta \omega_\beta/c$, where r_β is the amplitude of the electron oscillation. When $K \gg 1$ (regime for our experimental condition[21]), the on-axis X-ray radiation has a synchrotron-like spectrum,[8] characterized by $d^2I/dEd\Omega|_{\theta=0} \propto (E/E_c)^2 \mathcal{K}^2_{2/3}(E/E_c)$. The critical energy is defined as $E_c = 3\hbar K \gamma^2 \omega_\beta$, and $\mathcal{K}_{2/3}$ is the modified Bessel function of the second kind. The properties of the X-ray emission therefore depend on the accelerated electrons beam charge, energy, and oscillation amplitude, and through these quantities, on the plasma density. For instance, Fig. 5 shows the X-ray images corresponding to the shots of Fig. 3 at two different plasma densities. Figure 5(a) shows that no X-ray was detected for the low density case: although the electron energy is relatively high for this shot, the associated beam charge was too low to generate a signal on the CCD. On the contrary, as seen in Fig. 5(b), a strong X-ray signal was measured for the shot at higher plasma density owing to a higher beam charge. The different filters can be clearly seen, together with the grid supporting them. The round structure near the edges of the image is due to the filters holder blocking the edges of the beam.

The photon energy was quantitatively determined using the transmissions of the X-ray beam through different metals, and a least squares method.[11] For each metallic filter i, the theoretical camera response is calculated as the product of the filter transmission, $T_i(E)$, the transmission of 5 mm of air and 300 μm of beryllium, $T(E)$, and the CCD quantum efficiency $Q(E)$, as $C_i^{the} = \int \frac{d^2I}{dEd\Omega} T_i(E) T(E) Q(E)\, dE$. Assuming a synchrotron like spectrum, and minimizing the difference between theoretical and experimental camera responses for different filters, $\sum_i (C_i^{the} - C_i^{exp})^2$, gives the best fit of critical energy E_c. For the case of Fig. 5(b) obtained in a 10 mm long, 178 μm diameter capillary tube, the critical energy was evaluated to be 5.4 keV at $n_e \simeq 8 \times 10^{18}\,\mathrm{cm}^{-3}$.

Figure 6 shows that betatron X-ray radiation can be tuned by varying the plasma density. In this case, the X-ray fluence peaks at $5.7 \times 10^5\,\mathrm{ph/mrad}^2$ for $n_e \simeq 8 \times 10^{18}\,\mathrm{cm}^{-3}$ and behaves similarly as the beam charge given in Fig. 4(b). At lower plasma densities, the electron number decreases rapidly, so the photon number diminishes accordingly. If the

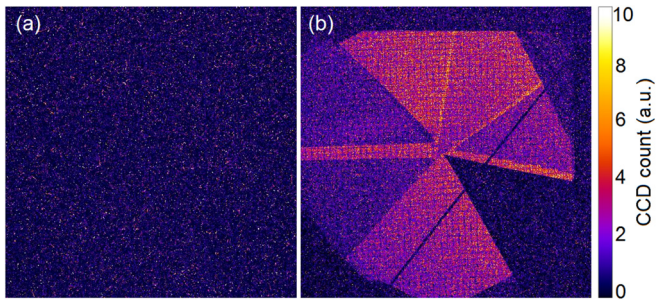

FIG. 5. X-ray beam images recorded on the X-ray CCD equipped with the set of metallic pieces described in the text; images (a) and (b) correspond to the shots of Figs. 3(a) and 3(c), respectively.[21]

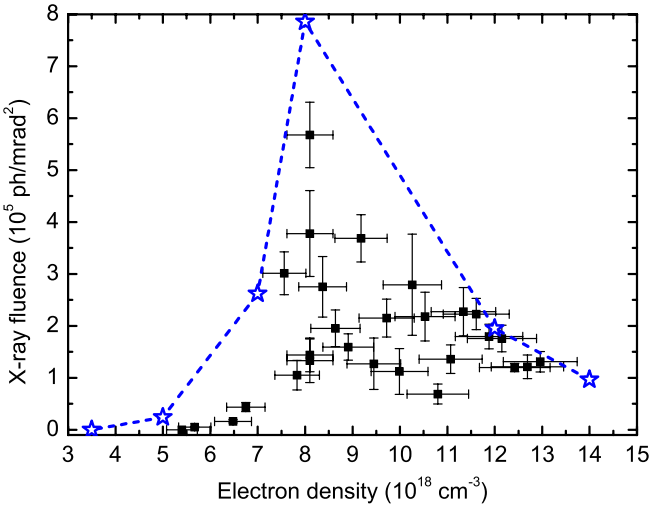

FIG. 6. X-ray fluence as a function of plasma electron density corresponding to the electron beams shown in Fig. 4. Each black square corresponds to one laser shot, blue stars represent the results obtained from 3D PIC simulation.

beam charge is too low, the X-ray signal finally vanishes, as seen in Fig. 5(a). Above the optimum density, the beam charge does not increase, while electron energy becomes lower as laser pump depletion length and the dephasing length shorten, which also leads to a drop of X-ray signal. This dependence of X-ray fluence on plasma density is well reproduced by simulation results, plotted as blue stars in Fig. 6.

Betatron X-ray radiation is also a powerful tool to investigate the acceleration process because of its strong dependence on the electron properties.[19,20,29] Figure 7 illustrates how the X-ray profile measured at the exit of capillary tubes can be used to determine the volume and locations inside the plasma where electrons are accelerated. X-rays are emitted as soon as electrons are trapped and wiggle in the plasma bubble. X-rays generated at different longitudinal positions inside the capillary tube will exit with an aperture cone determined by the capillary diameter, and the distance from the capillary exit. For an extended emission region inside the plasma, the X-ray image will exhibit a transition zone of varying intensity, which can be directly related to the length of the electron acceleration region inside the plasma.[19,20] In the following calculation, the X-ray source is assumed to be one dimensional, as its transverse size is of the order of a few microns and can be neglected compared to the typical longitudinal extension of the emission process (∼mm).

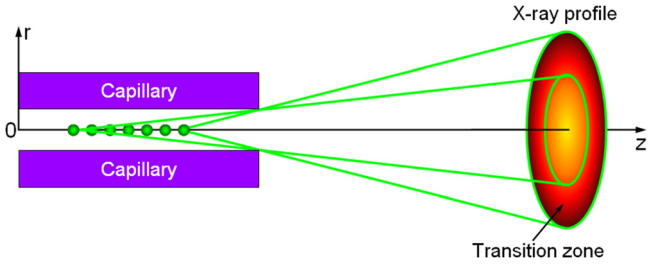

FIG. 7. Schematic illustration of the relation between the intensity distribution of the X-rays in the detector plane and the emission region inside a capillary tube.

Using the cylindrical coordinates illustrated in Fig. 7, the longitudinal profile of betatron emission $dI_X(z)/dz$ can be determined from the X-ray signal measured in the detector plane, $S(r,\theta)$, using[29]

$$\frac{dI_X(z)}{dz} = -\frac{1}{2\pi}\int_0^{2\pi} \frac{\partial S(r(z),\theta)}{\partial r}\frac{r^2(z)}{r_{cap}L_X}\,d\theta, \qquad (1)$$

with $r(z) = r_{cap}L_X/(L_{cap}-z)$. $L_X \simeq 110$ cm is the distance from the capillary exit to the detection plane; r_{cap}, L_{cap} stand for capillary radius and length, respectively.

The X-ray source is closer to the capillary exit when a short capillary tube is used, which geometrically produces a larger aperture shadow. For example, most of the shadow of the 10 mm long, 178 μm diameter capillary was beyond the X-ray detector size, as shown in Fig. 8(a). Only roughly a quarter of the beam going through the capillary could be recorded. As the shortest capillary tube studied, $L_{cap} = 10$ mm, is longer than the whole distance of laser evolution and electron acceleration (see Figs. 11 and 12), the X-ray emission due to electron trapping and acceleration is expected to be the same for a longer capillary tube. In order to determine the X-ray profile, a 30.5 mm long capillary tube was employed, for which all the X-ray beam confined by the capillary exit could be recorded, like in Fig. 8(b). The observed beam consists of a nearly homogeneous background together with a bright feature which suggests special electron trajectories in the plasma.[30] Excluding the section of the beam containing a bright feature inside the capillary shadow in Fig. 8(b), the radial profile of the X-ray signal averaged over the azimuthal angle was calculated and plotted in Fig. 8(c). Substituting this profile into Eq. (1), the longitudinal distribution of X-ray emission was obtained and plotted in Fig. 8(d) for five successive shots. $z = 0$ corresponds to the capillary entrance. It shows that electrons start to generate detectable X-rays with photon energy

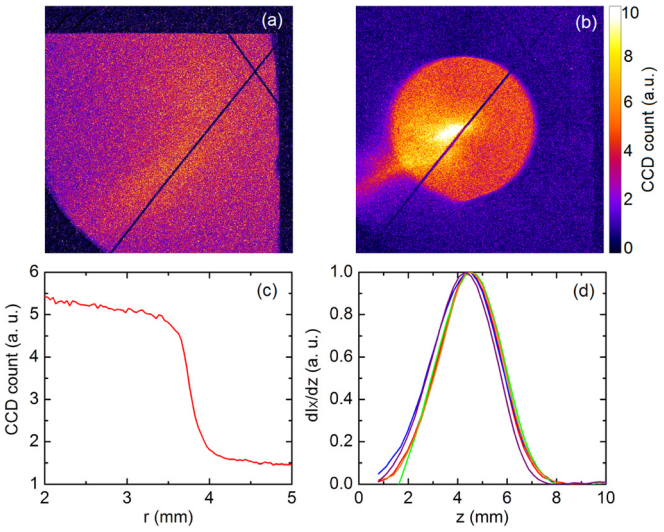

FIG. 8. X-ray beam distribution measured for $n_e = (8.1 \pm 0.5) \times 10^{18}$ cm^{-3} at the output of (a) a 10 mm long, 178 μm diameter capillary tube, (b) a 30.5 mm long, 178 μm diameter capillary tube; (c) averaged radial intensity of (b); (d) longitudinal profiles of X-ray emission, for five consecutive shots under the same conditions. The curves are normalized to their respective maxima.

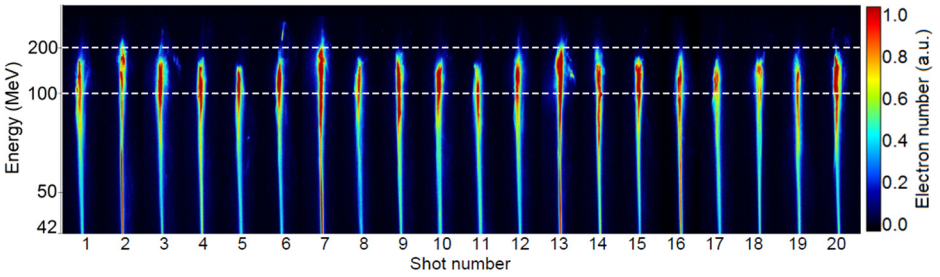

FIG. 9. Raw images of electron spectra for 20 consecutive shots measured at the output of a 10 mm long, 203 μm diameter capillary tube for $n_e = (7 \pm 0.4) \times 10^{18}$ cm^{-3}.

above 2 keV around $z \simeq 2$ mm. The photons become detectable (>2 keV) when the electron energy is higher than $\sim$50 MeV for the plasma density 8×10^{18} cm^{-3} and oscillation amplitude $r_\beta = 2\,\mu$m. After a distance corresponding to electron acceleration, the X-ray emission has a FWHM of about 3 mm, and peaks at $z \simeq 4.5$ mm, where the electrons reach their maximum energy, because the radiation power scales with γ^4. Afterwards, the X-ray emission decreases and stops at $z \simeq 7$ mm where the laser becomes too weak to sustain self-focusing (See Figs. 11 and 12). The precision of the above analysis is limited by the beam transverse source size. For the position of the emission peak at $z = 4.5$ mm, a beam size $r_\beta = 2\,\mu$m will result in the same intensity gradient on the detector as does a longitudinal emission extending $\sim$600 μm, which sets the resolution of the determination of the emission position.

D. Electrons and x-rays stability

Figure 6 shows that the X-ray fluence exhibits large shot-to-shot fluctuations. These fluctuations may be due to the process of electron injection, determining beam charge, or acceleration conditions, determining the electrons energy. Both effects contribute to the X-ray intensity, as shown in Sec. II C, where the X-ray distribution was used to characterize the acceleration process. In Fig. 8(d), the calculated longitudinal profiles of X-ray emission indicate a similar position and distance of X-ray emission for consecutive shots, which can be related to similar processes of electron acceleration. Thus, it can be assumed that the origin of the fluctuations lies more in the trapping conditions, and the amount of injected charge.

In order to get some insight on the origin of fluctuations, the stability of electrons and X-rays was examined. Figure 9 displays the electron spectra of 20 consecutive shots obtained with a 10 mm long, 203 μm diameter capillary tube. The plasma density was $n_e = (7 \pm 0.4) \times 10^{18}$ cm^{-3}, where strong signals could be obtained for both electrons and X-rays. For these parameters, electron injection occurred for every shot. On average, $\sim$45 pC electrons were accelerated to a maximum energy of $\sim$150 MeV.

For electrons, the measured maximum energy $\mathcal{E}_{max}$ (147 $\pm$ 12 MeV) and the mean energy $\bar{\mathcal{E}}_e$ (91 $\pm$ 7 MeV) both exhibit stability with standard deviation of 8%. The beam charge shows a shot-to-shot fluctuation of 17%. The percentages indicated in this section are the ratios of standard deviation over mean. The critical energy of X-ray shows a fluctuation of about 9%, and the X-ray fluence fluctuation was measured to be 12%. Note that these X-rays constitute the most intense on-axis part, measured by the detector with a small collecting angle, which may have smaller fluctuations than the total X-ray beam.

Figure 10 shows the measured X-ray fluence as a function of the measured beam charge, and a linear fit of the data. The slope of the linear fit is calculated to be 7.8×10^{-4} ph/mrad^2 per electron. The scaling developed for betatron radiation in ion channels[31] shows that the average number of photons emitted by an oscillating electron is given by $N_X \simeq 5.6 \times 10^{-3} N_\beta K$, where N_β is the number of betatron oscillations performed by the electron. The opening solid angle of the betatron radiation,[8] $\Omega = K/\gamma^2$, can be used to evaluate the strength parameter. The number of photons per solid angle can therefore be theoretically estimated to be $N_X/\Omega \simeq 5.6 \times 10^{-9} \gamma^2 N_\beta$ in unit of ph/mrad^2 per electron. By measuring electron energy, γ was evaluated as the average value plus/minus three times standard deviation to be $\gamma = 183 \pm 40$. Using the value of the slope of the linear fit in Figure 10, the number of electron oscillations is calculated to be $N_\beta \simeq 4 \pm 2$. From the experimental results in Fig. 10, we are thus able to estimate that the electron fulfills about four oscillations in the plasma. This finding is in reasonable agreement with the determined $N_\beta \simeq 5$ in PIC simulation for $n_e = 7 \times 10^{18}$ cm^{-3}.

The instability of beam charge is probably largely due to the process of electron self-injection. In the blow-out regime, the dynamics of electron self-injection is a complex process dependent on the laser non-linear evolution,[27] the bubble dynamics,[7] and beam loading.[32] As a result, a slight change to one of these processes, due, for example, to fluctuations of the laser energy distribution at the entrance of the plasma,

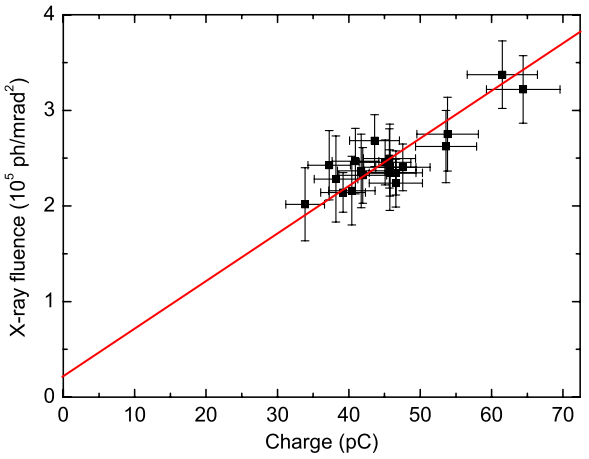

FIG. 10. X-ray fluence as a function of beam charge for the 20 shots shown in Fig. 9, where the red line is a linear fit.

will subsequently induce a large variation of beam charge, and consequently of the X-ray fluence. Stabilizing the electron beam charge would thus be a way to reduce shot-to-shot fluctuations and improve X-ray stability. The beam charge has been observed to be a considerably unstable parameter of the electron bunches produced in LWFA. Typically, the relative variation of beam charge (standard deviation/mean) is >50% for commonly used gas jets,[33] 16% for gas cell,[17] and down to 20% for advanced optical injection techniques.[34] Although there is no corresponding study on X-ray stability in the literature, it is still reasonable to stress that X-ray stability would be improved by controlling beam charge with some sophisticated approach, like the recent staged acceleration with separated nozzle injector[35] which showed that the charge stability can be reduced to 6% by small changes to the density profile.

III. SIMULATIONS

Simulations were performed with the 3D PIC code CALDER-CIRC.[22] Parameters were chosen close to experimental ones: a FWHM 40 fs laser pulse was taken as input condition with a normalized intensity of $a_0 = 1.6$, and the transverse profile measured experimentally as shown in Fig. 2(b). In the experiment, the laser focus in vacuum was set inside the capillary at 1 mm from the capillary entrance. A similar condition was studied in the simulation and compared to focusing position at 2.5 mm from the entrance. The gas density profile inside the capillary tubes is constant over the length situated between the two slits and decreases from the slits positions to the ends of the capillary tube. Numerical simulations using the commercial code FLUENT were performed to determine the gas distribution in the capillary tube and the density profile between the slits and the capillary exit.[23] For PIC simulations, the density profiles were simply assumed to be linearly increasing from 0 to a constant value of density, n_e, over a length of 3 mm, as shown in Figs. 11(a) and 12(a); the capillary entrance is located at $z = 0$ mm and the density plateau is assumed to start at $z = 2.5$ mm. The betatron radiation was calculated from Lineard-Wiechert potentials[8] by post-processing the trajectories of electrons with energies larger than 10 MeV. More details regarding the PIC simulation can be found in Ref. 20.

Simulations were carried out for different plasma electron densities and compared to experimental results. Whereas in the experiment the laser was focused 1 mm inside capillary tubes, it was found that simulations results are in better agreement with experiments for the simulation with focus at $z = 2.5$ mm, as can be seen in Figs. 4 and 6 where simulation results are plotted as blue stars. This sensitivity to focusing position is linked to laser propagation and evolution in the plasma. In the remaining part of this section, the behavior of the laser beam intensity, electron beam energy, and X-ray emission are examined along the capillary axis and the two cases of focus positions are compared for the case of $n_e = 8 \times 10^{18}$ cm^{-3}, at which both electrons and X-rays were systematically studied in experiment.

In the case of Fig. 11, after entering the plasma, the laser central bulk quickly self-focuses, and the normalized laser

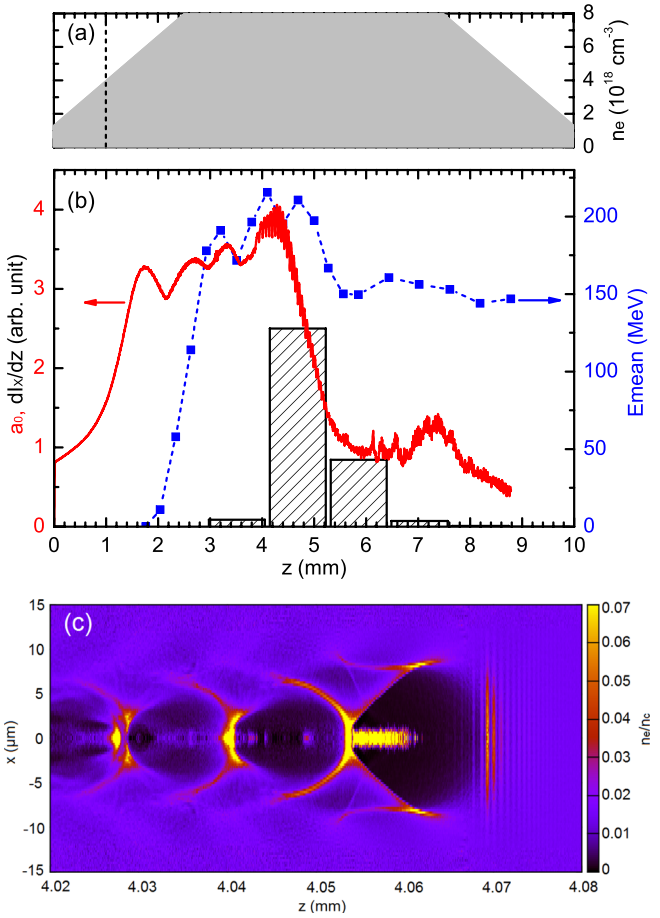

FIG. 11. Simulation results for $a_0 = 1.6$, and a background electron density $n_e = 8 \times 10^{18}$ cm^{-3}. (a) Density profile used in 3D PIC simulation with laser focus position in vacuum at $z = 1$ mm, indicated by a vertical dashed line. (b) Evolution of the normalized laser intensity (red solid line) and the mean energy (dashed blue line) of the electron bunch accelerated in the first plasma bucket. The histogram corresponds to the amplitude of X-ray emission in arbitrary unit. (c) Snapshot of plasma density around the position $z = 4.05$ mm, the laser propagates from left to right.

intensity increases up to $a_0 > 3$ at $z \simeq 1.7$ mm. With the help of capillary guiding and self-focusing, the laser propagates with a stable amplitude until $z \simeq 4.4$ mm. When most of the laser energy is transferred to the plasma wave, the laser becomes subsequently too weak to maintain self-focusing. This simulation result agrees well with the theoretical prediction[7] of laser pump depletion length $L_{dpl} \simeq 2.6$ mm. Closely following the laser pulse, a bubble with a radius of $\sim 7\ \mu$m is created, as illustrated in Fig. 11(c). An appreciable number of electrons starts to be trapped by the bubble after the first maximum of laser normalized intensity $z \simeq 2$ mm in Fig. 11(c), and the trapped electrons gain energy rapidly. The mean energy of the electron bunch produced in the first plasma bucket reaches a maximum of 215 MeV at $z \simeq 4.1$ mm and then decreases, because the electrons enter a decelerating phase. In addition, the laser intensity remains large enough ($a_0 > 3$) to trap electrons[33] over a few millimeters, so multiple electron trapping is seen in the simulation.

The betatron radiation produced by the electron beam is synchrotron-like but differs from the standard synchrotron spectrum given by $(E/E_c)^2 \mathcal{K}^2_{2/3}(E/E_c)$. That is because the accelerated electrons are widely-spread in energy and have

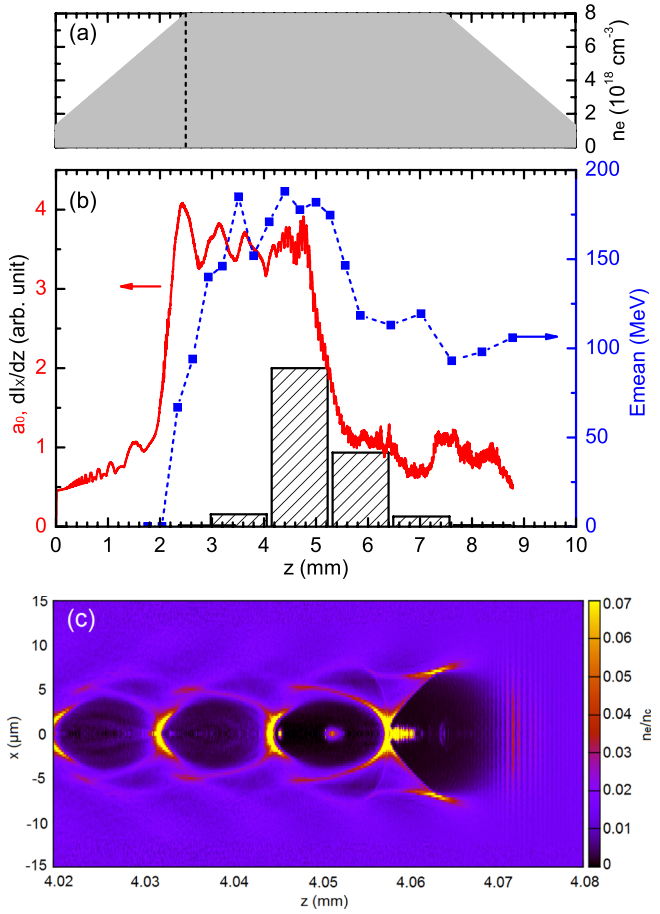

FIG. 12. Same as Fig. 11 with laser focus position in vacuum at z = 2.5 mm.

different oscillation amplitudes. Fitting the simulated spectrum with a standard synchrotron spectrum yields a critical energy of 7.7 keV, however, the simulated and the fitted spectra have a large difference in photon energy distribution. Therefore, it is more significant to define the critical energy E_c as the energy below or above which half power is radiated.[20] Accordingly E_c is 4.6 keV for this simulation case. The histogram in Fig. 11(b) represents the X-ray intensity, obtained by integrating photons from 1 to 10 keV, emitted at different longitudinal positions calculated over each 1 mm. It is seen that the X-ray generation extends from about $z = 3$ mm to around $z = 7.5$ mm and peaks at $z \simeq 4.6$ mm. This is in excellent agreement with the experimental observation presented in Fig. 8(d).

Simulations show that the X-ray pulse duration is ~35 fs at $n_e = 8 \times 10^{18}$ cm^{-3}, and the X-ray source radius was calculated to be[21] ~2 μm, which yields an X-ray peak brightness of the order of $\sim 1 \times 10^{21}$ ph/s/mm^2/mrad^2/0.1%BW. To our knowledge, this is the brightest X-ray source obtained with a 16 TW laser. Under the same laser conditions, the X-ray peak brightness is reduced by nearly two orders of magnitude when the capillary tube is replaced by a 2 mm gas jet,[21] because higher plasma densities are required to self-trap electrons over the length of the gas jet. Using a longer gas jet or a gas cell would also increase the X-ray brightness, but the use of a capillary tube enhances this effect by collecting the unfocused laser energy and reflecting it back to the axis.

The influence of the laser focus position can be evaluated by comparing Figs. 11 and 12. In Fig. 12, the laser focus position is located at the beginning of the density plateau and this leads to a faster self-focusing with a higher peak amplitude than in the case of Fig. 11. Then the laser amplitude oscillates with larger peak to peak amplitude. Electron injection occurs at about the same position $z \simeq 2$ mm, but the maximum value of the mean electron energy is higher in the case of Fig. 11 probably due to an increasing laser intensity from $z = 1.8$ to 4.5 mm. The X-ray emission shows a similar peak position around $z = 4.7$ mm. It can also be noticed in Fig. 12(c) that the number of electrons is lower in the first bucket after the laser pulse, which is essentially linked to different electron trapping processes dependant on laser evolution.

IV. CONCLUSION

In conclusion, electron acceleration by laser wakefield and the associated betatron radiation inside capillary tubes were experimentally studied with a 40 fs, 16 TW laser. Capillary tubes were used to collect the laser energy outside the focal spot central peak and assist laser self-focused over several millimeters. Operating in the blow-out regime, tens of pC electrons were accelerated up to ~300 MeV, and the X-ray peak brightness was estimated to be $\sim 1 \times 10^{21}$ ph/s/mm^2/mrad^2/0.1%BW, comparable to modern synchrotron light sources.

The X-ray emission was measured to be correlated to the accelerated electron beam charge. Therefore the production of a reliable beam charge would benefit future developments and applications of this table-top X-ray source. Moreover, the X-ray profile was used to investigate the acceleration process. This diagnostic provides a deeper insight of the physics of electron acceleration in long plasmas and can be compared to simulations. PIC simulations performed with parameters close to the experimental ones provide results in good agreement with experimental results. The agreement of the X-ray emission profile and location between simulation and experiment shows that the analysis of the X-ray emission is a powerful diagnostics, providing also information on the electron beam dynamics.

A comparison of two PIC simulations with different focus positions highlights the sensitivity of the laser propagation to the coupling conditions at the entrance of the plasma. Other parameters like the specific profile of density ramp, and the position and angle of the laser spot at the entrance of the capillary,[36] should also be taken into account in future simulations as well as in experiments, as they may be key parameters for improving the reliability of laser plasma accelerators.

ACKNOWLEDGMENTS

This experiment was funded by LASERLAB-EUROPE with Contract No. 228334, the Lund University X-ray Center (LUXC), the Swedish Research Council (including the Linné grant to LLC), and the Kunt and Alice Wallenberg Foundation. J. Ju acknowledges financial support from the Chinese Scholarship Council (CSC).

[1]T. Tajima and J. Dawson, Phys. Rev. Lett. **43**, 267 (1979).
[2]E. Esarey, C. B. Schroeder, and W. P. Leemans, Rev. Mod. Phys. **81**, 1229 (2009).
[3]S. P. D. Mangles, C. D. Murphy, Z. Najmudin, A. G. R. Thomas, J. L. Collier, A. E. Dangor, E. J. Divall, P. S. Foster, J. G. Gallacher, C. J. Hooker, D. A. Jaroszynski, A. J. Langley, W. B. Mori, P. A. Norreys, F. S. Tsung, R. Viskup, B. R. Walton, and K. Krushelnick, Nature **431**, 535 (2004).
[4]C. G. R. Geddes, Cs. Toth, J. van Tilborg, E. Esarey, C. B. Schroeder, D. Bruhwiler, C. Nieter, J. Cary, and W. P. Leemans, Nature **431**, 538 (2004).
[5]J. Faure, Y. Glinec, A. Pukhov, S. Kiselev, S. Gordienko, E. Lefebvre, J.-P. Rousseau, F. Burgy, and V. Malka, Nature **431**, 541 (2004).
[6]W. P. Leemans, B. Nagler, A. J. Gonsalves, Cs. Tóth, K. Nakamura, C. G. R. Geddes, E. Esarey, C. B. Schroeder, and S. M. Hooker, Nat. Phys. **2**, 696 (2006).
[7]W. Lu, M. Tzoufras, C. Joshi, F. S. Tsung, W. B. Mori, J. Viera, R. A. Fonseca, and L. O. Silva, Phys. Rev. ST Accel. Beams **10**, 061301 (2007).
[8]E. Esarey, B. A. Shadwick, P. Catravas, and W. P. Leemans, Phys. Rev. E **65**, 056505 (2002).
[9]A. G. R. Thomas, Phys. Plasmas **17**, 056708 (2010).
[10]A. Rousse, K. T. Phuoc, R. Shah, A. Pukhov, E. Lefebvre, V. Malka, S. Kiselev, F. Burgy, J.-P. Rousseau, D. Umstadter, and D. Hulin, Phys. Rev. Lett. **93**, 135005 (2004).
[11]S. Kneip, C. McGuffey, J. L. Martins, S. F. Martins, C. Bellei, V. Chvykov, F. Dollar, R. Fonseca, C. Huntington, G. Kalintchenko, A. Maksimchuk, S. P. D. Mangles, T. Matsuoka, S. R. Nagel, C. A. J. Palmer, J. Schreiber, K.-Ta. Phuoc, A. G. R. Thomas, V. Yanovsky, L. O. Silva, K. Krushelnick, and Z. Najmudin, Nat. Phys. **6**, 980 (2010).
[12]M. Schnell, A. Savert, B. Landgraf, M. Reuter, M. Nicolai, O. Jackel, C. Peth, T. Thiele, O. Jansen, A. Pukhov, O. Willi, M. C. Kaluza, and C. Spielmann, Phys. Rev. Lett. **108**, 075001 (2012).
[13]G. R. Plateau, C. G. R. Geddes, D. B. Thorn, M. Chen, C. Benedetti, E. Esarey, A. J. Gonsalves, N. H. Matlis, K. Nakamura, C. B. Schroeder, S. Shiraishi, T. Sokollik, J. van Tilborg, Cs. Toth, S. Trotsenko, T. S. Kim, M. Battaglia, Th. Stohlker, and W. P. Leemans, Phys. Rev. Lett. **109**, 064802 (2012).
[14]F. Wojda, K. Cassou, G. Genoud, M. Burza, Y. Glinec, O. Lundh, A. Persson, G. Vieux, E. Brunetti, R. P. Shanks, D. Jaroszynski, N. E. Andreev, C.-G. Wahlström, and B. Cros, Phys. Rev. E **80**, 066403 (2009).
[15]B. Cros, C. Courtois, G. Matthieussent, A. Di Bernardo, D. Batani, N. Andreev, and S. Kuznetsov, Phys. Rev. E **65**, 026405 (2002).
[16]D. P. Umstadter, Nature Photon. **5**, 576 (2011).
[17]J. Osterhoff, A. Popp, Zs. Major, B. Marx, T. P. Rowlands-Rees, M. Fuchs, M. Geissler, R. Horlein, B. Hidding, S. Becker, E. A. Peralta, U. Schramm, F. Gruner, D. Habs, F. Krausz, S. M. Hooker, and S. Karsch, Phys. Rev. Lett. **101**, 085002 (2008).
[18]H. E. Ferrari, A. Lifschitz, and B. Cros, Plasma Phys. Controlled Fusion. **53**, 014005 (2011).
[19]G. Genoud, K. Cassou, F. Wojda, H. E. Ferrari, C. Kamperidis, M. Burza, A. Persson, J. Uhlig, S. Kneip, S. P. D. Mangles, A. Lifschitz, B. Cros, and C.-G. Wahlstrom, Appl. Phys. B **105**, 309 (2011).
[20]H. E. Ferrari, A. F. Lifschitz, G. Maynard, and B. Cros, Phys. Plasmas **18**, 083108 (2011).
[21]J. Ju, K. Svensson, A. Dopp, H. E. Ferrari, K. Cassou, O. Neveu, G. Genoud, F. Wojda, M. Burza, A. Persson, O. Lundh, C.-G. Wahlstrom, and B. Cros, Appl. Phys. Lett. **100**, 191106 (2012).
[22]A. F. Lifschitz, X. Davoine, E. Lefebvre, J. Faure, C. Rechatin, and V. Malka, J. Comput. Phys. **228**, 1803 (2009).
[23]J. Ju and B. Cros, J. Appl. Phys. **112**, 113102 (2012).
[24]Y. Glinec, J. Faure, A. Guemnie-Tafo, V. Malka, H. Monard, J. P. Larbre, V. De Waele, J. L. Marignier, and M. Mostafavi, Rev. Sci. Instrum. **77**, 103301 (2006).
[25]A. Buck, K. Zeil, A. Popp, K. Schmid, A. Jochmann, S. D. Kraft, B. Hidding, T. Kudyakov, C. M. S. Sears, L. Veisz, S. Karsch, J. Pawelke, R. Sauerbrey, T. Cowan, F. Krausz, and U. Schramm, Rev. Sci. Instrum. **81**, 033301 (2010).
[26]S. Kneip, S. R. Nagel, S. F. Martins, S. P. D. Mangles, C. Bellei, O. Chekhlov, R. J. Clarke, N. Delerue, E. J. Divall, G. Doucas, K. Ertel, F. Fiuza, R. Fonseca, P. Foster, S. J. Hawkes, C. J. Hooker, K. Krushelnick, W. B. Mori, C. A. J. Palmer, K. Ta Phuoc, P. P. Rajeev, J. Schreiber, M. J. V. Streeter, D. Urner, J. Vieira, L. O. Silva, and Z. Najmudin, Phys. Rev. Lett. **103**, 035002 (2009).
[27]D. H. Froula, C. E. Clayton, T. Doppner, K. A. Marsh, C. P. J. Barty, L. Divol, R. A. Fonseca, S. H. Glenzer, C. Joshi, W. Lu, S. F. Martins, P. Michel, W. B. Mori, J. P. Palastro, B. B. Pollock, A. pak, J. E. Ralph, J. S. Ross, C. W. Siders, L. O. Silva, and T. Wang, Phys. Rev. Lett. **103**, 215006 (2009).
[28]C. M. Huntington, A. G. R. Thomas, C. McGuffey, T. Matsuoka, V. Chvykov, G. Kalintchenko, S. Kneip, Z. Najmudin, C. Palmer, V. Yanovsky, A. Maksimchuk, R. P. Drake, T. Katsouleas, and K. Krushelnick, Phys. Rev. Lett. **106**, 105001 (2011).
[29]S. Corde, C. Thaury, K.Ta Phuoc, A. Lifschitz, G. Lambert, J. Faure, O. Lundh, E. Benveniste, A. Ben-Ismail, L. Arantchuk, A. Marciniak, A. Stordeur, P. Brijesh, A. Rousse, A. Specka, and V. Malka, Phys. Rev. Lett. **107**, 215004 (2011).
[30]K. T. Phuoc, S. Corde, R. Shah, F. Albert, R. Fitour, J.-P. Rousseau, F. Burgy, B. Mercier, and A. Rousse, Phys. Rev. Lett. **97**, 225002 (2006).
[31]I. Kostyukov, S. Kiselev, and A. Pukhov, Phys. Plasmas **10**, 4818 (2003).
[32]C. Rechatin, J. Faure, X. Davoine, O. Lundh, J. Lim, A. Ben-Ismail, F. Burgy, A. Tafzi, A. Lifschitz, E. Lefebvre, and V. Malka, New J. Phys. **12**, 045023 (2010).
[33]S. P. D. Mangles, A. G. R. Thomas, O. Lundh, F. Lindau, M. C. Kaluza, A. Persson, C. G. Wahlstrom, K. Krushelnick, and Z. Najmudin, Phys. Plasmas **14**, 056702 (2007).
[34]J. Faure, C. Rechatin, A. Norlin, F. Burgy, A. Tafzi, J.-P. Rousseau, and V. Malka, Plasma Phys. Controlled Fusion **49**, B395 (2007).
[35]A. J. Gonsalves, K. Nakamura, C. Lin, D. Panasenko, S. Shiraishi, T. Sokollik, C. Benedetti, C. B. Schroeder, C. G. R. Geddes, J. van Tilborg, J. Osterhoff, E. Esarey, C. Toth, and W. P. Leemans, Nat. Phys. **7**, 862 (2011).
[36]M. Veysman, N. E. Andreev, K. Cassou, Y. Ayoul, G. Maynard, and B. Cros, J. Opt. Soc. Am. B **27**, 1400 (2010).